

Research paper

Ultrastrong and damage-tolerant ceramic architectures via 3D printing



Rong Wang ^{a,1}, Haitao Ye ^{a,b,1}, Jianxiang Cheng ^a, Honggeng Li ^a, Pengfei Zhu ^c, Bo Li ^d, Rong Fan ^b, Juzheng Chen ^b, Yang Lu ^{b,e}, Qi Ge ^{a,*}

^a Department of Mechanical and Energy Engineering, Southern University of Science and Technology, Shenzhen 518055, China

^b Department of Mechanical Engineering, City University of Hong Kong, Kowloon, the Hong Kong Special Administrative Region of China

^c Foshan (Southern China) Institute for New Materials, Foshan, China

^d Institute of Materials Research, Tsinghua Shenzhen International Graduate School, Shenzhen 518055, China

^e Nano-Manufacturing Laboratory (NML), Shenzhen Research Institute of City University of Hong Kong, Shenzhen, China

ARTICLE INFO

ABSTRACT

Keywords:

Damage tolerance
Ceramic architectures
3D printing
Mechanical property
In situ compression

Ceramic materials have high mechanical strength and exceptional environmental stability, but are suboptimal for structural applications due to their inherent brittleness and low damage tolerance. Here, we report ultrastrong and damage-tolerant ceramic architectures that are designed based on Schwarz Primitive structures and manufactured by digital light processing (DLP)-based 3D printing. Through micro-computed tomography imaging and *in situ* compression experiments, we reveal that the step effect of 3D printing plays a role in crack initiation and propagation of the 3D-printed architectures. When the loading direction is perpendicular to the printing direction, the steps can induce cracks to propagate along the loading direction, which is beneficial to localize the cracks in the outer part of structure and enhance the structural strength and damage tolerance. After optimizing structural design and heat treatment process, the printed ceramic architecture can achieve compressive strength as high as 710 MPa at a relative density of 57.58 %. More importantly, the printed ceramic architecture exhibits excellent damage tolerance. It can bear more 20 cycles of 6 % compressive strain when 28 % of the structures have been damaged. The ceramic architecture can still bear the load without failure even when the degree of damage reaches 44 %. The superior mechanical properties make them have great potential in engineering applications that require high mechanical reliability.

1. Introduction

Ceramic materials have found numerous applications in aerospace [1], electronic industry [2,3], biomedical engineering [4] and other fields [5–7] due to their high strength, high stiffness and remarkable environmental stability. In particular, the excellent thermal and chemical stability make them the best candidate materials for the applications in extreme conditions such as high-temperature [8–10] and corrosive environments [11]. However, ceramics are generally sensitive to cracks because of their inherent brittleness and low fracture toughness. Compared with metals and polymers, it is more difficult to prepare and process ceramics, during which various cracks or flaws are easily introduced, resulting in poor mechanical performance. Especially for complex cellular ceramic structures, even slight defects may lead to severe deterioration of their mechanical properties. Therefore, ceramic components commonly suffer from sudden fracture and catastrophic

failure, which brings enormous safety hazards and excludes their application from the fields requiring high reliability.

To improve the toughness and damage resistance of ceramics, many efforts have been focused on design and fabrication of bioinspired composite materials [12–16] including the brick-and-mortar structures inspired from the natural nacre of mollusk shells [17–19], the planar twisted plywood structures inspired from lobster claw [20,21], and the bone-like structures [22]. However, in most of these cases, the toughening mechanism originates from the introduction of polymeric ductile phase, which makes the prepared ceramic/polymer composites unable to be used at high temperature. Moreover, the commonly used preparation techniques, such as ice templating [23], freeze casting [22] and simple assembly of engraved ceramic sheets [17,19], are time-consuming and not suitable for large-scale manufacturing, which limit the scope of their practical applications.

The creation of mechanical metamaterials [24–26] is another

* Corresponding author.

E-mail address: geq@sustech.edu.cn (Q. Ge).

¹ These authors contributed equally to this work.

effective way to overcome brittleness. Ultralight hollow-tube ceramic micro/nanolattices have been fabricated by high-precision 3D printing technique combined with atomic layer deposition (ALD) [27–29]. The thickness of the hollow tubes is tens of nanometers. These micro-/nanolattices could deform largely via shell buckling, and exhibit ductile behavior. Due to the size effect, the mechanical properties of materials in nanoscale are much better than that in macroscale. Polymer-derived ceramic nanoarchitectures with feature size of ~200 nm have been manufactured by two-photon polymerization (TPP) and subsequent pyrolysis, and exhibit ductility and ultrahigh strength compared with those structures at the millimeter scale [30]. However, the overall size of these nanolattices is limited to the scale of ~20 μm. Although various millimeter- and centimeter-scale cellular structures with enhanced mechanical properties have also been reported in recent years [31–35], most of them have low strength less than 100 MPa, and their capacities of damage resistance are still far from being desired. How to improve the mechanical properties of ceramic structures at millimeter and centimeter scales remains a significant challenge.

Here, we report ultrastrong and damage-tolerant ceramic architectures via 3D printing. We directly fabricate Schwarz Primitive [36] ceramic structures with dimensions in centimeters via digital light processing (DLP)-based high-precision 3D printing. Through optimized structural design and preparation process, the compressive strength of the ceramic structures has reached as high as 710 MPa at the relative density of 57.58 %, which is the highest compared with previously reported cellular structures. More importantly, we find that the structural mechanical properties are anisotropic due to the step effect of 3D printing: the compressive strength in the transverse direction (perpendicular to the printing direction) is 20–70 % higher than that in the longitudinal direction (parallel to the printing direction). When the applied load is perpendicular to the printing direction, the steps induce cracks to propagate directionally along the loading direction in the outer part of the structures, which causes the structures to break gradually and avoids the sudden collapse. Thus, the strength of 3D-printed ceramic structures can be improved significantly. Moreover, they can bear the repeated load 20 times when 28 % of the structures have been damaged. Even though damaged as much as 44 %, they can still bear the load without failure. The ultrahigh strength, excellent cyclic performance and damage tolerance make them great potential for practical engineering applications.

2. Materials and methods

2.1. Preparation of photosensitive ceramic slurry

3 mol % yttria-stabilized ZrO₂ ceramic powders (6.08 g/cm³, d₅₀ = 0.56 μm, Shenzhen Adventuretech Co., Ltd., China), 1,6-hexanediol diacrylate (HDDA, Bide Pharmatech Ltd., China), polyethylene glycol diacrylate (PEGDA, M_w = 400, Innochem Technology Co., Ltd., China) were used as raw materials. Diphenyl(2,4,6-trimethylbenzoyl) phosphine oxide (TPO, Bide Pharmatech Ltd., China) was used as photo-initiator and KOS110 (Guangzhou Kangoushuang Trade Co., Ltd., China) as dispersant. Firstly, HDDA, PEGDA and ZrO₂ were mixed with a weight ratio of 4:1:20. 5 wt % of dispersant (relative to ZrO₂) and 0.5 wt % of TPO (relative to resin) were added to the mixture. Then the mixture was milled at 540 rpm for 12 h in a planetary ball mill (F-P400E, Hunan Focucy Experimental Instrument Co., Ltd., China). Finally, homogeneous photosensitive ZrO₂ slurry with solid loading of ~40 vol % was obtained.

2.2. Fabrication of ceramic Schwarz P structures

We printed all the ZrO₂ structures on a self-built DLP-based ceramic 3D printing apparatus with the layer thickness of 100 μm and energy dose of 36 mJ/cm². The wavelength of UV light is 405 nm. After printing, the green parts were heated at 550 °C for 4 h with the heating

rate of 0.25 °C/min in Ar₂ for debinding, and then sintered at 1450 °C for 2 h with the heating rate of 1 °C/min in air to obtain the ceramic parts. A tube furnace (GSL-1700X, Hefei Kejing, China) and muffle furnace (KSL-1700X, Hefei Kejing, China) were used to perform the debinding and sintering processes, respectively. The detailed heat treatment process can be found in the *Supplementary Materials* (Figs. S1 and S2). The original size of as-printed structures with 5 × 5 × 5 units is 10 mm × 10 mm × 10 mm. After sintering, the samples have a size of ~7.25 mm × 7.25 mm × 7.25 mm, corresponding to a linear shrinkage ratio of 27.5 %. The snapshot of the 3D-printed green body and the samples after heat treatment is shown in *Supplementary Fig. S3*.

2.3. Microstructural characterization

Morphological observations were conducted on a field emission scanning electron microscope (SUPRA55, ZEISS, Germany) with a 5 kV accelerating voltage. Prior to SEM observation, samples were sputtered with platinum for 30 s using a vacuum coater (Leica EM ACE200, Leica Microsystems, Germany).

Micro-computed tomography (Micro-CT) imaging was conducted using ZEISS 3D X-ray microscope (Xradia 520 Versa, ZEISS, Germany) with X-ray source voltage of 160 kV, current of 62.5 μA and exposure time of 6 s. We scanned samples with voxel size resolution of 10 μm. The acquired tomography datasets were reconstructed using Dragonfly software (Object Research Systems). The 3D distribution of cracks in the damaged samples was obtained utilizing the Dragonfly's segmentation toolkit.

2.4. Mechanical test

Uniaxial compression experiments were performed using MTS machine (Model E45, MTS Systems Corporation, USA) equipped with a 50 kN load cell under a crosshead speed of 0.45 mm/min (corresponding strain rate of 0.1 %/s) at room temperature. The samples were compressed in transverse direction and longitudinal direction respectively until failure to obtain the strength in the two directions. Three samples of each group were tested. We used load of 28 kN for transverse compression and 18.5 kN for longitudinal compression to obtain the partially damaged samples, which were used for micro-CT imaging. For the cyclic compression tests, the loading-unloading cycles were repeated 20 times under three different strains (4 %, 5 % and 6 %). For the gradient loading-unloading test, the sample was measured under different strains ranging from 1 % until failure.

In order to observe the crack initiation and propagation directly, in situ compression tests were conducted through the use of Deben Microtest 200 N stage placed in the chamber of FEI Quanta450 FEG SEM (FEI company, Hillsboro, OR, USA). Single unit cell with the size of ~0.725 mm × 0.725 mm × 0.725 mm was tested at a crosshead speed of 0.2 mm/min. SEM images and videos were taken synchronously.

2.5. Finite element analysis

To simulate the failure of 3D printed brittle ZrO₂ ceramics, we use the brittle cracking model available in the commercial finite element software ABAQUS/Explicit (V6.14, Dassault Systèmes Simulia Corp., USA). This model is useful for modeling materials such as ceramics, glasses, or brittle rocks. A simple Maximum stress criterion (Rankine Criterion) is used to detect crack initiation. This criterion states that a crack forms when the maximum principal tensile stress exceeds the tensile strength of the brittle material. The elastic properties and post-failure stress-strain behavior of ceramic were obtained from the three-point bending tests, and the element would be deleted once its strength was decreased to zero. Solid 10-node modified tetrahedron (C3D10M) element was used to mesh all the parts. The material model setting is the same for all of the TPMS structures.

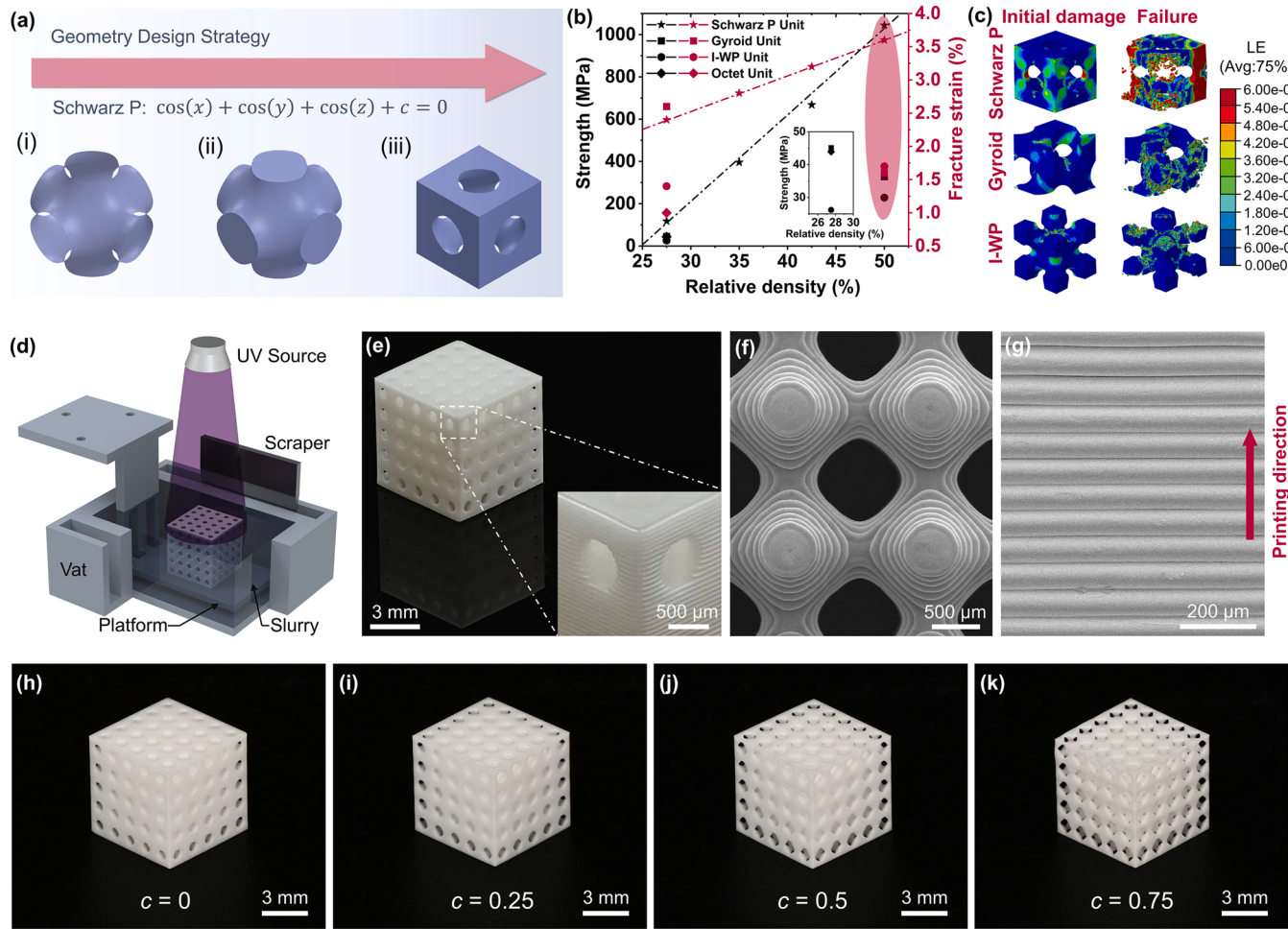


Fig. 1. Design, fabrication and microstructure of the TPMS ceramics. (a) Schematic diagram of geometry design strategy of Schwarz P unit cell. (i) P surface unit, (ii) Positive phase of solid-based P unit via enclosing the P surface, (iii) The desired negative phase of P unit in this work. (b) Comparison of compressive strength and fracture strain of three different TPMS units (Schwarz P unit, Gyroid unit and I-WP unit) and octet-truss unit with different relative densities as predicted by FEA simulations. (c) FEA results of principal strain contours for three TPMS units (relative density of 50 %) under the initial and failure damage. The colorbar presents the value of strain. (d) Illustration of the DLP-based ceramic 3D printing apparatus. (e) Snapshot of the 3D-printed ZrO_2 Schwarz P structure with $5 \times 5 \times 5$ units after sintering. (f) and (g) SEM images of the cross section (f) and side wall (g) of the 3D-printed ZrO_2 Schwarz P structure. (h-k) Snapshots of Schwarz P samples with different structural parameters after sintering.

3. Results and discussion

3.1. Design and fabrication strategy

Triply Periodic Minimal Surface (TPMS) structures are a special class of 3D cellular structures defined by mathematical methods [37,38]. The minimal surface is smooth and continuous surface with zero mean curvature at each point, which could avoid stress concentration. This characteristic makes TPMS structures exhibit superior physical and mechanical properties [39,40] than that of the strut-based architectures such as Kelvin foam and octet-truss [35]. The Schwarz Primitive structure, one of the well-known TPMS structures, was first mentioned by German mathematician Schwarz in 1865 [36]. Different from the usual sheet-based TPMS structure produced by thickening the minimal surface [41,42], we construct solid-based Schwarz P structure in this work. The design strategy is shown in Fig. 1(a). The approximation equation of Schwarz P surface could be expressed as $\cos X + \cos Y + \cos Z + c = 0$, where $X = 2\pi x/a$, $Y = 2\pi y/a$, $Z = 2\pi z/a$, a is the unit cell parameter and c is a constant. A typical P surface unit is shown in Fig. 1(a)(i). Positive phase of solid P unit (Fig. 1a(ii)) is created by enclosing the P surface. The desired negative phase (Fig. 1a(iii)) is generated by subtracting the positive phase from its bounding cubic box. Schwarz P structures with

different volume fractions or relative densities can be obtained by changing the constant c . To demonstrate the superiority of Schwarz P structure, we calculated the mechanical properties of three different TPMS unit (Schwarz P, Gyroid and I-WP) cells as well as octet-truss unit with different relative densities $\bar{\rho}$ ($\bar{\rho} = \rho/\rho_s$, where ρ is the density of structure and ρ_s is the density of parent solid material) by finite element analysis (FEA), as shown in Fig. 1(b). The compressive strength and fracture strain of Schwarz P unit increase linearly with relative density. At the same relative density of 50 %, the compressive strength of Schwarz P unit is 3–4 times over that of Gyroid and I-WP units. The principal strain contours in Fig. 1(c) show the strain distribution of three TPMS unit cells under the initial and failure damage. The Schwarz P unit cell has more uniform distribution of strain, so it could withstand more loads and is not prone to failure. Whereas, the other two structures have concentrated strain in localized areas, causing relatively poor load capacity. Therefore, the Schwarz P structure exhibits the best mechanical properties among the four types of structures.

As shown in Fig. 1(d), we print zirconia (ZrO_2) Schwarz P structures on a self-built DLP-based ceramic 3D printing apparatus. The UV light engine projects masked images to photopolymerize the ceramic slurry, and 3D objects are constructed in a top-down, layer-by-layer manner, where the scraper is used to coat the slurry uniformly. The 3D-printed

Table 1

Designed and real $\bar{\rho}$ of 3D-printed Schwarz P structures with $5 \times 5 \times 5$ units.

Parameter c	0	0.25	0.50	0.75
Designed $\bar{\rho}$	50 %	42.86 %	35.7 %	28.5 %
Real $\bar{\rho}$	57.58 %	50.16 %	42.82 %	34.89 %

green body is a composite of ceramic powder and polymer matrix, which could be converted to a pure ceramic structure after debinding and sintering processes. Fig. 1(e) shows the photograph of a sintered Schwarz P structure with clearly visible step effect. The layered pattern could be observed more obviously from the scanning electron microscope (SEM) images of the cross section and sidewall as shown in Fig. 1(f) and (g), respectively. In this work, Schwarz P structures with four different relative densities $\bar{\rho}$ are designed and fabricated. The sintered samples are shown in Fig. 1(h-k). The specific parameters are listed in Table 1. The real $\bar{\rho}$ are slightly higher than designed $\bar{\rho}$ due to some extent of overexposure in the printing process. As the c value increases from 0 to 0.75, the real $\bar{\rho}$ of the structure decreases from 57.58 % to 34.89 %.

3.2. Mechanical properties

Uniaxial compression tests of ZrO_2 Schwarz P structure were performed in two different loading directions, as shown in Fig. 2(a). We define the loading direction that parallels to the printing direction as longitudinal direction, and the direction that is perpendicular to the printing direction as transverse direction. Fig. 2(b) shows the typical stress-strain curves of Schwarz P structures with different $\bar{\rho}$ when the load is applied in longitudinal direction. The structures have high

compressive strength and fracture strain. The compressive strength of structures with $\bar{\rho}$ of 57.58 % reaches 418 MPa. All the stress-strain plots present a good linear relationship, indicating that elastic deformation occurs in the whole compression process until structural failure. The compressive strength decreases gradually as $\bar{\rho}$ decreases. Interestingly, the mechanical properties of 3D-printed Schwarz P structures exhibit obvious anisotropy. When compressed in the transverse direction, the structures exhibit ultrahigh mechanical properties (Fig. 2(c)). The compressive strength of structures with $\bar{\rho}$ of 57.58 % reaches as high as 710 MPa. Fig. 2(d) shows the comparison of compressive strength in different loading directions. The specific data are listed in Supplementary Table S1. It is evident that the strength in transverse direction (σ_T) is higher than that in longitudinal direction (σ_L) for all the samples. For the structures with $\bar{\rho}$ of 57.58 %, σ_T is 1.70 times over σ_L . For the structures with $\bar{\rho}$ of 34.89 %, σ_T/σ_L decreases to only 1.20. As the relative density $\bar{\rho}$ decreases, the ratio σ_T/σ_L decreases obviously, indicating that the mechanical anisotropy is weakened with the decrease in $\bar{\rho}$. Furthermore, different from the relatively smooth curves in Fig. 2(b), two or three small fluctuations appear on the stress-strain curves in Fig. 2(c). Each of these fluctuations implies some damages occurred during the transverse loading process. In other words, under the transverse load, these 3D-printed Schwarz P structures were damaged gradually rather than suddenly collapsed.

3.3. Mechanism analysis of crack initiation and propagation

In order to analyze the origin of ultrastrong mechanical properties of these 3D-printed ZrO_2 Schwarz P structures, we conducted micro-CT imaging and in situ compression experiments. Structures with

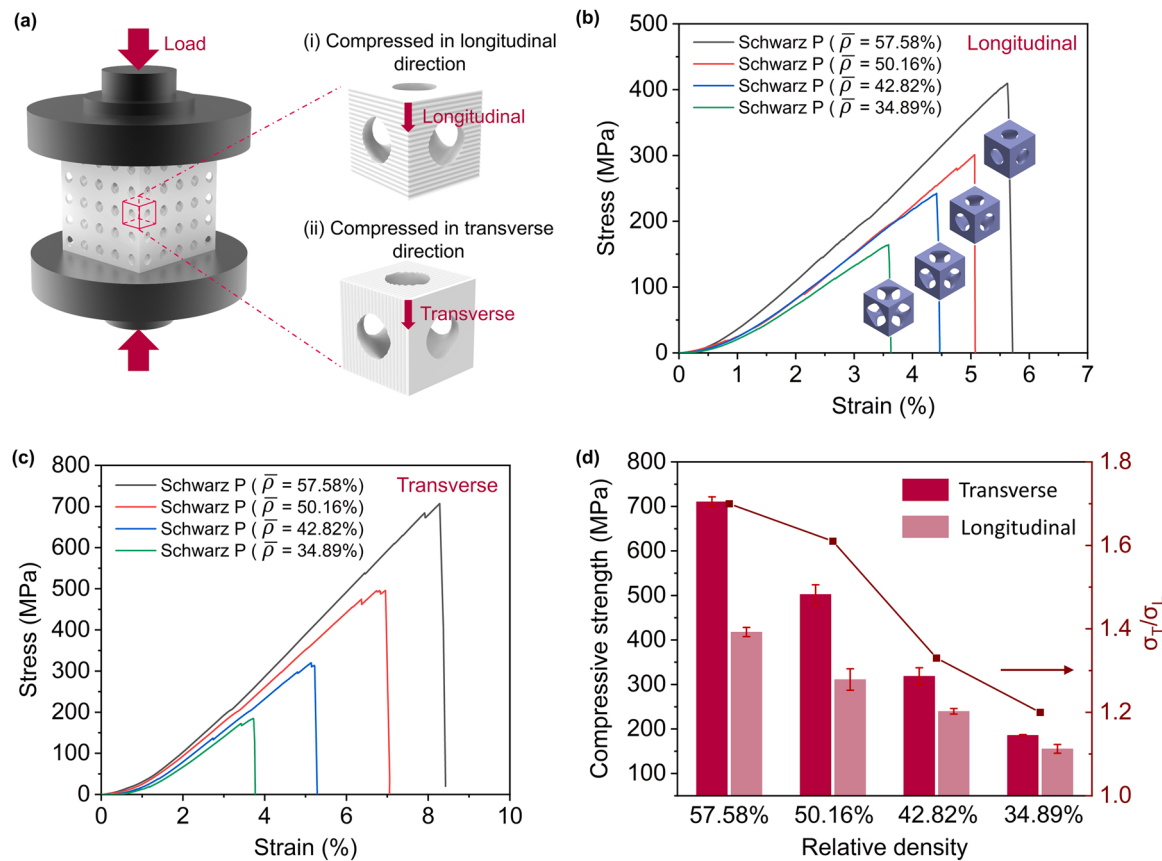


Fig. 2. Mechanical properties of 3D-printed ZrO_2 Schwarz P structures ($5 \times 5 \times 5$ units). (a) Illustration of the compression test with two different loading directions. (b) and (c) Stress-strain plots of structures with varying $\bar{\rho}$ when compressed in longitudinal direction (b) and transverse direction (c), respectively. The insets show the images of single Schwarz P unit cell with varying $\bar{\rho}$. (d) Comparison of their compressive strength in the two loading directions. σ_T/σ_L is the ratio of transverse strength to longitudinal strength.

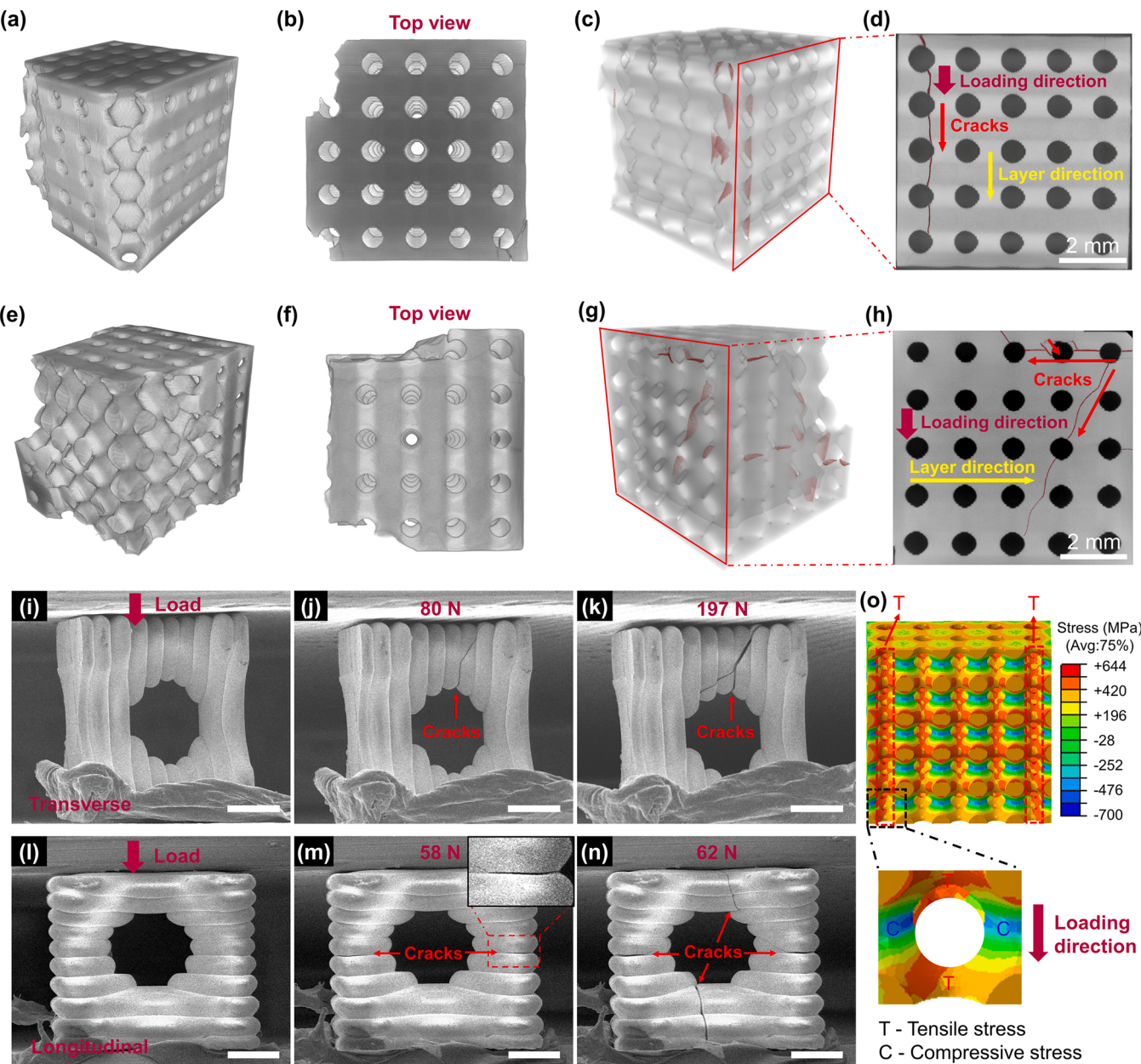


Fig. 3. Characterization and mechanism analysis of crack initiation and propagation. (a-d) Micro-CT 3D reconstructed images of Schwarz P structure ($\bar{\rho} = 57.58\%$) after compressed by the load of 28 kN in transverse direction: Perspective view (a), top view (b), 3D crack distribution image (c) and 2D sectional image (d). (e-h) Micro-CT 3D reconstructed images of Schwarz P structure ($\bar{\rho} = 57.58\%$) after compressed by the load of 18.5 kN in longitudinal direction: Perspective view (e), top view (f), 3D crack distribution image (g) and 2D sectional image (h). The dark red shadow areas in (c, d, g and h) indicate the cracks. (i-n) In situ compression experiments under transverse load (i-k) and longitudinal load (l-n), respectively. Scale bars in (i-n): 200 μm . (o) FEA result of stress contour on Schwarz P structure sectioned from the middle. Tensile and compressive stress points are marked on the enlarged image of a unit cell. The red dashed areas indicate the maximum tensile stress distribution areas.

$5 \times 5 \times 5$ units ($\bar{\rho} = 57.58\%$) were compressed by a load of 28 kN in transverse direction (~75 % of the failure load) and 18.5 kN in longitudinal direction (~85 % of the failure load), respectively. Micro-CT 3D reconstructed images show the 3D morphology of partially damaged samples and distribution of main cracks. When the load is applied in transverse direction, the vertical edges of the sample are damaged; the cracks are localized in the edge units and distributed along the loading direction (Fig. 3(a-d) and Video S1). When the load is applied in longitudinal direction, the vertical surfaces of the sample are damaged; the cracks are distributed along the layer direction and even obliquely penetrating the entire structure (Fig. 3(e-h) and Video S2), which will result in premature failure of the structure.

Supplementary material related to this article can be found online at doi:10.1016/j.addma.2022.103361.

In the in situ compression experiments, we can observe the initiation and propagation of cracks directly. Here, we used single unit cell with the size of $0.725 \text{ mm} \times 0.725 \text{ mm} \times 0.725 \text{ mm}$ for in situ compression experiments with a maximum load of 200 N. Fig. 3(i-k) and Video S3 show the detailed process of crack initiation and propagation under the transverse load. A crack initiates from the step caused by 3D printing. Then, the crack extends along the loading direction to a certain length and deflects at an angle of ~45°. Although the crack penetrates the upper part, the structure will not fail. During the whole transverse compression experiment, there is only one crack that extends at a

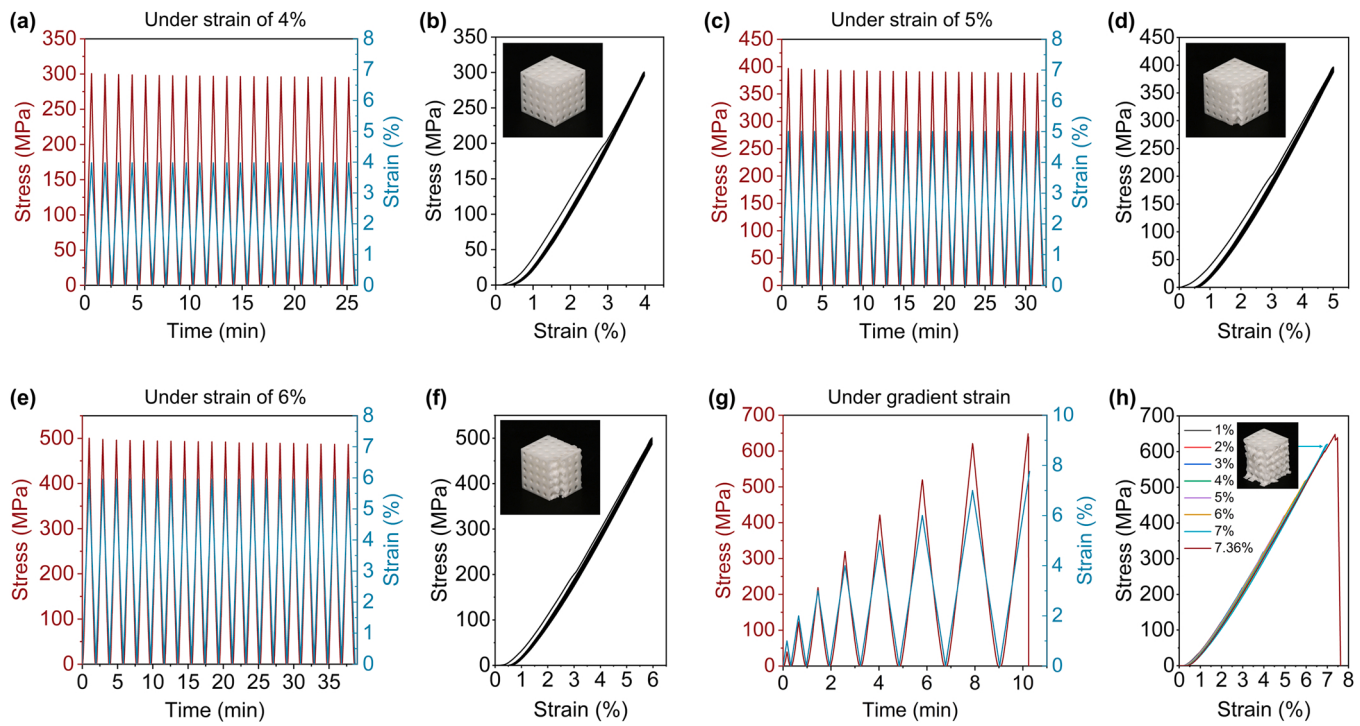


Fig. 4. Multicycle compression test results of ZrO_2 Schwarz P structures ($\bar{\rho} = 57.58\%$) loaded in transverse direction. (a) and (b) 20 cycles under the maximum strain of 4 %. (c) and (d) 20 cycles under the maximum strain of 5 %. (e) and (f) 20 cycles under the maximum strain of 6 %. (g) and (h) Gradient loading experiment where the maximum strain for each loading-unloading cycle increases from 1 % to 7.36 %. The insets show the samples after the cyclic compression tests under strain of 4 % (b), 5 % (d), 6 % (f) and 7 % (h), respectively.

relatively slow speed, and the rest of the unit cell is intact, which will not lead to sudden failure. Whereas, the sample behaves totally differently when the longitudinal load is applied (Fig. 3(l-n) and Video S4). Two cracks perpendicular to the loading direction initiate and extend along the steps on the left and right sides. As the load increases, another two cracks initiate at the upper and lower parts and propagate along the loading direction rapidly. The penetration of these four cracks results in overall failure of the unit cell.

Supplementary material related to this article can be found online at doi:10.1016/j.addma.2022.103361.

As shown in Fig. 3(o), FEA simulation presents the stress contour on the Schwarz P structure, which is sectioned from the middle for better presentation. According to FEA result, we take one unit cell as an example to denote the tensile stress points and the compressive stress points. The upper and lower parts of the unit cell endure tensile stress, while the left and right parts endure compressive stress. Since the compressive strength of ceramic is much greater than the tensile strength, fractures occur at the maximum tensile stress points. For the entire structure, the maximum tensile stress points are distributed along the loading direction at the vertical edge units, where the red dashed areas denote T in Fig. 3(o). Thus, the vertical edges are damaged first, which is consistent with the phenomenon observed in the experiment.

Combining the above experiment and simulation results, we conclude that the anisotropic property of 3D-printed Schwarz P structures is caused by the different mechanisms of crack initiation and propagation under different loading directions. The step effect that originates from the layer-by-layer stacking of 3D printing, is the key to generating mechanical anisotropy. The steps induce cracks to initiate and propagate along the layer direction. For transverse compression, the loading direction is parallel to the layer direction. Then, the step-induced cracks are parallel to the loading direction and localized in the vertical edge units. Even though the edges are damaged, the structures can still withstand greater load rather than sudden collapse. Thus, the structures exhibit ultrahigh compressive strength in transverse

direction. For longitudinal compression, the loading direction is perpendicular to the layer direction. Then, the steps induce cracks to propagate perpendicular to the loading direction. In the meantime, the applied load also induces some cracks parallel to the loading direction. That is, cracks initiate from multiple sites and propagate in multiple directions, which causes cracks to be distributed throughout the structure. The structures will fracture and collapse rapidly. Thus, the compressive strength in longitudinal direction is worse than that in transverse direction.

3.4. Cyclic performance

To evaluate the damage tolerance of the 3D-printed Schwarz P ceramic structure, we conducted cyclic uniaxial compression tests on the ceramic structures in transverse loading direction. These structures have relative density $\bar{\rho}$ of 57.58 % and strength σ_T of ~710 MPa. We define the degree of damage D_d as $D_d = N_d/N_{\text{total}}$, where N_d is the number of damaged units and N_{total} is the total number of units ($5 \times 5 \times 5$ in this case). As shown in Fig. 4(a), during 20 linear loading-unloading cycles under displacement control with the maximum strain of 4 % (corresponding to 42 % of σ_T), the stress on structure responds linearly, and the maximum stress (~300 MPa) decreases slightly with the increase in loading cycles. Fig. 4(b) confirms the excellent linear elasticity where the stress-strain curves basically coincide with each other except for the one under the first cycle. Moreover, there is no visible damage on the sample after the test. In Fig. 4(c) and (d), the sample is loaded for 20 cycles under the maximum strain of 5 % (corresponding to 55 % of σ_T). One vertical edge (corresponding to 5 units) is damaged after the first cycle, so that D_d is 4 %. During the subsequent cycles, it is not damaged further. In Fig. 4(e) and (f), the sample loaded for 20 cycles under the maximum strain of 6 % (corresponding to 69 % of σ_T) has similar mechanical behavior and D_d is 28 %. Fig. 4(g) and (h) present the gradient loading experiment where the maximum strain for each loading-unloading cycle gradually increases from 1 % to the fracture strain

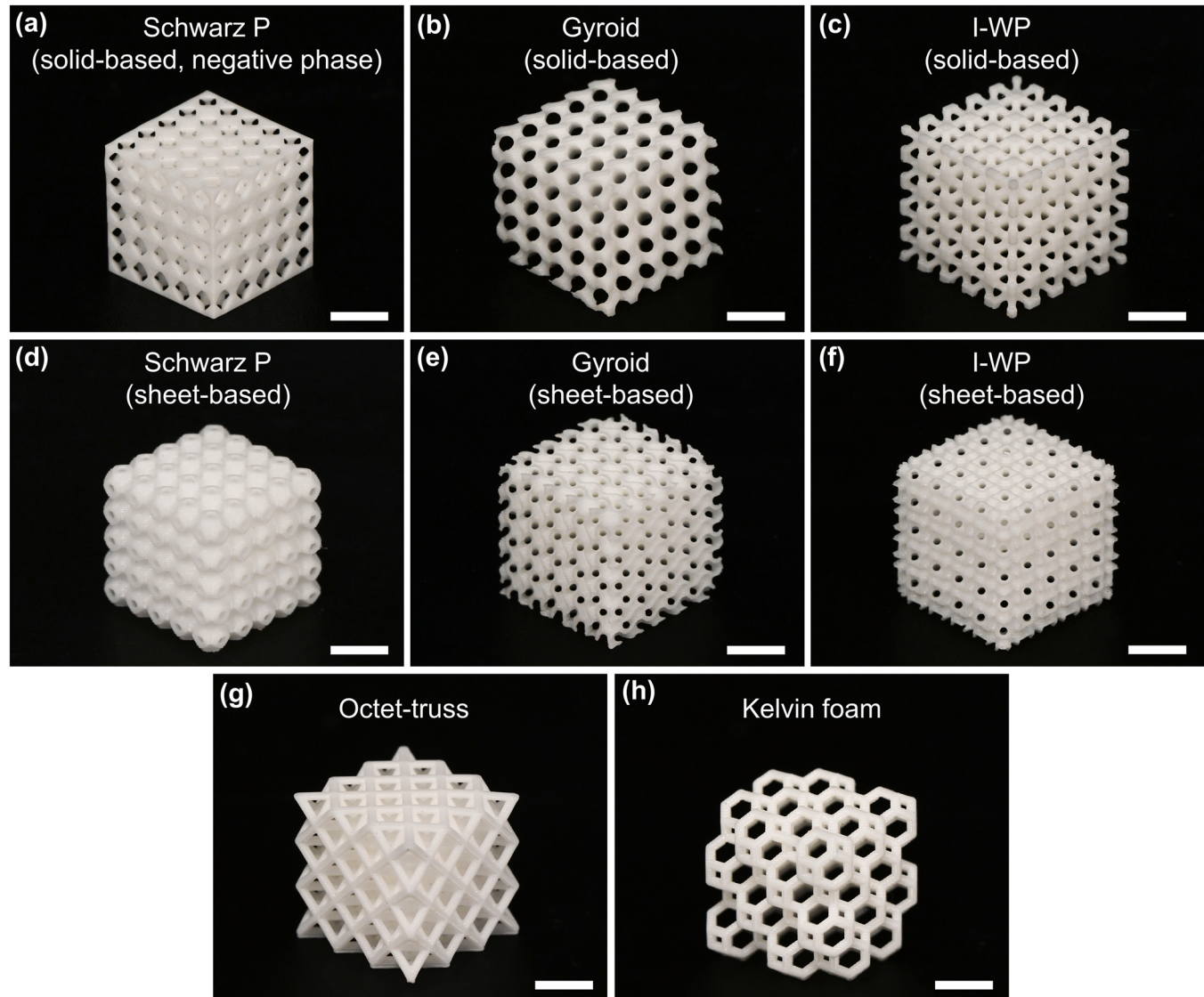


Fig. 5. Optical images of different ZrO_2 cellular structures. (a) Solid-based Schwarz P with $\bar{\rho}$ of 34.89 %. (b) Solid-based Gyroid with $\bar{\rho}$ of 30.62 %. (c) Solid-based I-WP with $\bar{\rho}$ of 29.90 %. (d) Sheet-based Schwarz P with $\bar{\rho}$ of 33.51 %. (e) Sheet-based Gyroid with $\bar{\rho}$ of 31.14 %. (f) Sheet-based I-WP with $\bar{\rho}$ of 30.27 %. (g) Octet-truss with $\bar{\rho}$ of 34.23 %. (h) Kelvin foam with $\bar{\rho}$ of 16.44 %. Scale bars: 3 mm.

(7.36 %). When the strain is greater than 4 %, the edge units of the sample begin to damage. After increasing the maximum strain to 7 % (corresponding to 87 % of σ_T), D_d reaches 44 %. The further increase in the loading strain makes the sample broken into small pieces with a maximum stress of 648 MPa, which is 91 % of σ_T . These cyclic loading-unloading experiments demonstrate excellent damage tolerance of the structure. It is gradually damaged with the increase in the applied load. A certain degree of damage does not lead to a sudden failure of the structure. The structure could still support load even if it is seriously damaged (D_d is up to 44 %). Compared with the brittle fracture failure of traditional ceramics, this 3D-printed structure has excellent damage tolerance, which can provide an early warning function to avoid catastrophic collapse in practical applications.

3.5. Comparison of mechanical properties of different cellular structures

In order to demonstrate the superior mechanical properties of our solid-based Schwarz P structures, we also printed solid-based Gyroid and I-WP structures, sheet-based Schwarz P, Gyroid and I-WP structures, as well as octet-truss and Kelvin foam. The optical images of sintered samples are shown in Fig. 5. These cellular structures have similar

overall size of $\sim 7.25 \text{ mm} \times 7.25 \text{ mm} \times 7.25 \text{ mm}$ and relative densities of 30–35 % except Kelvin foam.

Fig. 6(a) shows the typical stress-strain curves of four different cellular structures with similar relative densities, including solid-based Schwarz P, Gyroid and I-WP structures, as well as octet-truss. The loads are applied in transverse direction. The compressive strength of solid-based Schwarz P structure is 3.5 times that of solid-based Gyroid structure, 14 times that of solid-based I-WP structure, and 4.8 times that of octet-truss. This result is consistent with the FEA result in Fig. 1(b). Fig. 6(b) compares the transverse strength σ_T and longitudinal strength σ_L of all the 3D-printed cellular structures in this work. The transverse strength is always greater than the longitudinal strength for all the solid-based TPMS structures, sheet-based TPMS structures and non-TPMS structures (octet-truss and Kelvin foam). The specific data are listed in Supplementary Table S2. Among these cellular structures, the solid-based Schwarz P have the most superior mechanical properties.

Fig. 6(c) shows the relative compressive strength of our ZrO_2 Schwarz P structures in transverse direction versus relative density, compared with other recently reported ZrO_2 cellular ceramics [34,35]. The relative strength $\bar{\sigma}$ can be calculated by the equation $\bar{\sigma} = \sigma/\sigma_s$, where σ is the strength of structures and σ_s is the strength of parent solid

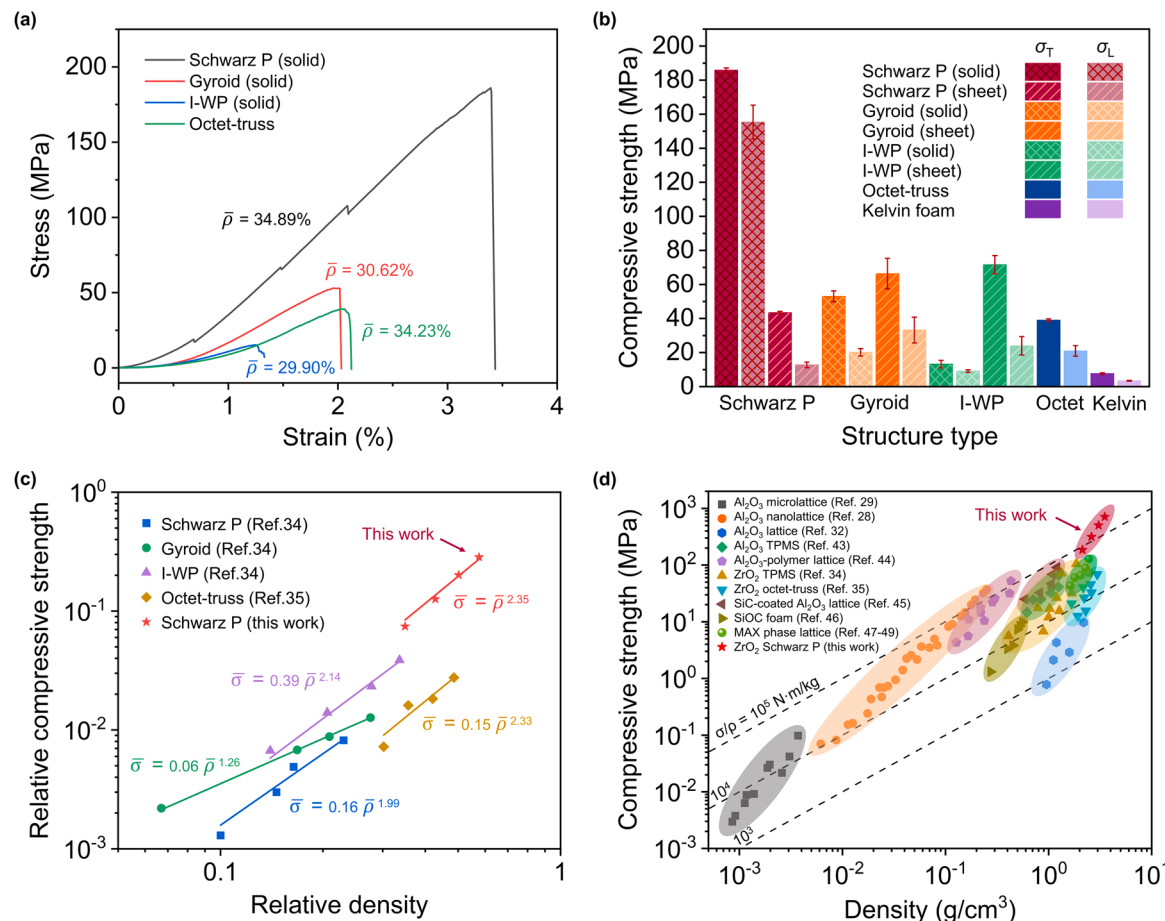


Fig. 6. Mechanical property plots of ZrO_2 Schwarz P and other cellular structures. (a) Typical stress-stain curves of solid-based Schwarz P, Gyroid and I-WP as well as octet-truss with similar relative densities of 30–35 % loaded in transverse direction. (b) Transverse compressive strength σ_T and longitudinal compressive strength σ_L of different structures, including solid-based and sheet-based Schwarz P, Gyroid, and I-WP structures, as well as octet-truss and Kelvin foam. (c) Relative compressive strength as a function of relative density for different ZrO_2 structures. (d) An Ashby chart plotting compressive strength versus density for previously reported cellular ceramics. Dotted lines indicate contours of constant strength-density ratio $C = \sigma/\rho$ (N·m/kg).

material. For cellular structures, the relation between relative strength $\bar{\sigma}$ and relative density $\bar{\rho}$ can be described as the equation: $\bar{\sigma} = K\bar{\rho}^n$, where K and n are experimental constants [29]. The scaling exponent n depends on the microstructure. The n of 1 indicates an ideal stretch-dominated deformation, and n of 2 typically indicates a bend-dominated deformation [29]. The relative strength of our structures can be fitted as $\bar{\sigma} = \bar{\rho}^{2.35}$ with K value of 1 and n of 2.35, indicating a bend-dominated deformation behavior. Our structures exhibit remarkably higher relative strength than the reported TPMS and octet-truss structures. Specially, the relative strength of our structure is twice as that of the reported I-WP structure under the similar $\bar{\rho}$ of ~35 % [34], and 7 times as that of the reported octet-truss structure under the similar $\bar{\rho}$ of ~43 % [35]. The Ashby chart in Fig. 6(d) compares the existing cellular ceramics [28,29,32–35,43–49], demonstrating that the structures created in this work reach a new height in the field of high-strength cellular ceramics at centimeter scale.

We mainly attribute the superior mechanical properties of our ceramic structures to the special structural design. The solid-based Schwarz P structures have much higher strength than the commonly used sheet-based Schwarz P structures, which is confirmed by the experimental data in Fig. 6(b). In addition, the heat treatment process also has a great influence on mechanical properties. A two-step process of debinding in Ar_2 and sintering in air with optimized heating rate was used to avoid defects as much as possible. We also conducted the one-step process of debinding and sintering both in air for comparison. The details of the two different heat treatment processes could be found

in [Supplementary Materials \(Figs. S1 and S2\)](#). From the SEM images in [Supplementary Fig. S4](#), we could clearly see that there are some cracks on the sample treated with the one-step thermal process while there are no obvious cracks on the sample treated with the two-step thermal process. The transverse strength of the Schwarz P structure ($\bar{\rho} = 57.58\%$) treated with the two-step thermal process is 1.82 times that of the sample treated with the one-step thermal process, as shown in [Supplementary Fig. S5](#). Thus, the optimized structural design and heat treatment process result in the ultrastong mechanical properties of ZrO_2 ceramic cellular structures in this work.

4. Conclusions

We have fabricated ultrastrong and damage-tolerant ZrO_2 Schwarz P structures via DLP 3D printing. Through optimized structural design and preparation process, their compressive strength has improved significantly compared with previously reported cellular ceramics. The strength of our structure with relative density of 57.58 % reaches as high as 710 MPa. Uniaxial compression tests show that our structures exhibit ultrahigh mechanical properties and obvious anisotropy. Micro-CT imaging and in situ compression experiments reveal the mechanisms of crack initiation and propagation under different loading directions. The step effect of 3D printing can induce the cracks to extend directionally. When loaded in transverse direction, the step-induced cracks propagate along the loading direction, which is beneficial to localize the cracks in the outer part of structure and enhance the mechanical properties. Thus,

the transverse strength is much higher than the longitudinal strength. Cyclic loading experiments demonstrate that these structures have excellent damage tolerance and can withstand more loads even if damaged as much as 44 %. The ultrastrong and damage-tolerant ceramic structures can reduce the risk of catastrophic collapse and have great potential in engineering applications.

CRediT authorship contribution statement

Chen Juzheng: Methodology, Investigation. **Fan Rong:** Resources, Investigation. **Li Bo:** Methodology, Investigation, Formal analysis. **Zhu Pengfei:** Resources, Investigation. **Wang Rong:** Writing – review & editing, Writing – original draft, Visualization, Methodology, Investigation, Data curation. **Ge Qi:** Writing – review & editing, Supervision, Resources, Project administration, Funding acquisition. **Lu Yang:** Writing – review & editing, Resources, Funding acquisition. **Ye Haitao:** Writing – original draft, Methodology, Investigation, Conceptualization. **Li Honggeng:** Methodology, Investigation. **Cheng Jianxiang:** Methodology, Investigation.

Declaration of Competing Interest

The authors declare that they have no known competing financial interests or personal relationships that could have appeared to influence the work reported in this paper.

Data Availability

Data will be made available on request.

Acknowledgements

This work was supported by the Key-Area Research and Development Program of Guangdong Province (grant no. 2020B090923003). R. W. thanks the financial support by the Science and Technology Plan of Shenzhen City (grant no. JCYJ20190813171603633). H.L. thanks the China Postdoctoral Science Foundation (grant no. 2021TQ0139). Y.L. thanks the support under the Shenzhen-Hong Kong-Macau Technology Research Program (Type C, SGDX2020110309300301). Q.G. acknowledges the supports by Technology Innovation Program (Grant #: 20009618, The Development of PAD Printer System for Micro LED Multi-Bonding Technology) funded By the Ministry of Trade, Industry & Energy (MOTIE, Korea).

Appendix A. Supporting information

Supplementary data associated with this article can be found in the online version at [doi:10.1016/j.addma.2022.103361](https://doi.org/10.1016/j.addma.2022.103361).

References

- [1] N.P. Padture, Advanced structural ceramics in aerospace propulsion, *Nat. Mater.* 15 (2016) 804–809.
- [2] F. Li, D. Lin, Z. Chen, Z. Cheng, J. Wang, C. Li, Z. Xu, Q. Huang, X. Liao, L.Q. Chen, T.R. Shrout, S. Zhang, Ultrahigh piezoelectricity in ferroelectric ceramics by design, *Nat. Mater.* 17 (2018) 349–354.
- [3] J. Li, Z. Shen, X. Chen, S. Yang, W. Zhou, M. Wang, L. Wang, Q. Kou, Y. Liu, Q. Li, Z. Xu, Y. Chang, S. Zhang, F. Li, Grain-orientation-engineered multilayer ceramic capacitors for energy storage applications, *Nat. Mater.* 19 (2020) 999–1005.
- [4] M. Zhang, R. Lin, X. Wang, J. Xue, C. Deng, C. Feng, H. Zhuang, J. Ma, C. Qin, L. Wan, J. Chang, C. Wu, 3D printing of Haversian bone-mimicking scaffolds for multicellular delivery in bone regeneration, *Sci. Adv.* 6 (2020) eaaz6725.
- [5] Z. Liu, T. Lu, F. Xue, H. Nie, R. Withers, A. Studart, F. Kremer, N. Narayanan, X. Dong, D. Yu, L. Chen, Y. Liu, G. Wang, Lead-free (Ag,K)NbO₃ materials for high-performance explosive energy conversion, *Sci. Adv.* 6 (2020) eaba0367.
- [6] C. Duan, R.J. Kee, H. Zhu, C. Karakaya, Y. Chen, S. Ricote, A. Jarry, E.J. Crumlin, D. Hook, R. Braun, N.P. Sullivan, R. O'Hayre, Highly durable, coking and sulfur tolerant, fuel-flexible protonic ceramic fuel cells, *Nature* 557 (2018) 217–222.
- [7] Y. Nakamura, Y. Sakai, M. Azuma, S.-i Ohkoshi, Long-term heat-storage ceramics absorbing thermal energy from hot water, *Sci. Adv.* 6 (2020) eaaz5264.
- [8] R.P. Wilkerson, B. Gludovatz, J. Ell, J. Watts, G.E. Hilmas, R.O. Ritchie, High-temperature damage-tolerance of coextruded, bioinspired ("nacre-like"), alumina/nickel compliant-phase ceramics, *Scr. Mater.* 158 (2019) 110–115.
- [9] E. Wuchina, E. Opila, M. Opeka, B. Fahrenholz, I. Talmi, UHTCs: ultra-high temperature ceramic materials for extreme environment applications, *Electrochim. Soc. Interface* 16 (2007) 30–36.
- [10] P.I.B.G. Pelissari, F. Bouville, V.C. Pandolfelli, D. Carnelli, F. Giuliani, A.P. Luz, E. Saiz, A.R. Studart, Nacre-like ceramic refractories for high temperature applications, *J. Eur. Ceram. Soc.* 38 (2018) 2186–2193.
- [11] S. Baitalik, N. Kayal, Thermal shock and chemical corrosion resistance of oxide bonded porous SiC ceramics prepared by infiltration technique, *J. Alloy. Compd.* 781 (2019) 289–301.
- [12] H.Y. Sarvestani, D.A. van Egmond, I. Esmail, M. Genest, C. Paquet, B. Ashrafi, Bioinspired stochastic design: tough and stiff ceramic systems, *Adv. Funct. Mater.* 32 (2022) 2108492.
- [13] A.R. Studart, Additive manufacturing of biologically-inspired materials, *Chem. Soc. Rev.* 45 (2016) 359–376.
- [14] U.G.K. Wegst, H. Bai, E. Saiz, A.P. Tomsia, R.O. Ritchie, Bioinspired structural materials, *Nat. Mater.* 14 (2015) 23–36.
- [15] X. Yan, B. Bethers, H. Chen, S. Xiao, S. Lin, B. Tran, L. Jiang, Y. Yang, Recent advancements in biomimetic 3D printing materials with enhanced mechanical properties, *Front. Mater.* 8 (2021), 518886.
- [16] R.O. Ritchie, The conflicts between strength and toughness, *Nat. Mater.* 10 (2011) 817–822.
- [17] Z. Yin, F. Hannard, F. Barthelat, Impact-resistant nacre-like transparent materials, *Science* 364 (2019) 1260–1263.
- [18] Y. Cheng, Y. An, Y. Liu, Q. Wei, W. Han, X. Zhang, P. Zhou, C. Wei, N. Hu, ZrB₂-based "brick-and-mortar" composites achieving the synergy of superior damage tolerance and ablation resistance, *ACS Appl. Mater. Interfaces* 12 (2020) 33246–33255.
- [19] A. Rahimizadeh, H.Y. Sarvestani, L. Li, J.B. Robles, D. Backman, L. Lessard, B. Ashrafi, Engineering toughening mechanisms in architected ceramic-based bioinspired materials, *Mater. Des.* 198 (2021), 109375.
- [20] S.-M. Chen, H.-L. Gao, Y.-B. Zhu, H.-B. Yao, L.-B. Mao, Q.-Y. Song, J. Xia, Z. Pan, Z. He, H.-A. Wu, S.-H. Yu, Biomimetic twisted plywood structural materials, *Natl. Sci. Rev.* 5 (2018) 703–714.
- [21] Y. An, Y. Yang, Y. Jia, W. Han, Y. Cheng, Mechanical properties of biomimetic ceramic with Bouligand architecture, *J. Am. Ceram. Soc.* 105 (2021) 2385–2391.
- [22] G. Singh, S. Soundarapandian, Bone-like structure by modified freeze casting, *Sci. Rep.* 10 (2020) 7914.
- [23] F. Bouville, E. Maire, S. Meille, B. Van de Moortèle, A.J. Stevenson, S. Deville, Strong, tough and stiff bioinspired ceramics from brittle constituents, *Nat. Mater.* 13 (2014) 508–514.
- [24] A.J.D. Shaikée, H. Cui, M. O'Masta, X.R. Zheng, V.S. Deshpande, The toughness of mechanical metamaterials, *Nat. Mater.* 21 (2022) 297–304.
- [25] J.U. Surjadi, Y. Lu, Design criteria for tough metamaterials, *Nat. Mater.* 21 (2022) 272–274.
- [26] J.U. Surjadi, L. Gao, H. Du, X. Li, X. Xiong, N.X. Fang, Y. Lu, Mechanical metamaterials and their engineering applications, *Adv. Eng. Mater.* 21 (2019) 1800864.
- [27] D. Jang, L.R. Meza, F. Greer, J.R. Greer, Fabrication and deformation of three-dimensional hollow ceramic nanostructures, *Nat. Mater.* 12 (2013) 893–898.
- [28] L.R. Meza, S. Das, J.R. Greer, Strong, lightweight, and recoverable three-dimensional ceramic nanolattices, *Science* 345 (2014) 1322–1326.
- [29] X. Zheng, H. Lee, T.H. Weisgraber, M. Shutteff, J. DeOtte, E.B. Duoss, J.D. Kuntz, M.M. Biener, Q. Ge, J.A. Jackson, S.O. Kucheyev, N. Fang, X. C.M. Spadaccini, Ultralight, ultrafast mechanical metamaterials, *Science* 344 (2014) 1373–1377.
- [30] J. Bauer, C. Crook, A. Guell Izard, Z.C. Eckel, N. Ruvalcaba, T.A. Schaedler, L. Valdevit, Additive manufacturing of ductile, ultrastrong polymer-derived nanoceramics, *Matter* 1 (2019) 1547–1556.
- [31] S.M. Sajadi, L. Vásárhelyi, R. Mousavi, A.H. Rahmati, Z. Kónya, Á. Kukovecz, T. Arif, T. Filletre, R. Vajtai, P. Boul, Z. Pang, T. Li, C.S. Tiwary, M.M. Rahman, P. M. Ajayan, Damage-tolerant 3D-printed ceramics via conformal coating, *Sci. Adv.* 7 (2021) eabc5028.
- [32] L. Sun, P. Dong, Y. Zeng, J. Chen, Fabrication of hollow lattice alumina ceramic with good mechanical properties by Digital Light Processing 3D printing technology, *Ceram. Int.* 47 (2021) 26519–26527.
- [33] Z. Li, Z. Chen, J. Liu, Y. Fu, C. Liu, P. Wang, M. Jiang, C. Lao, Additive manufacturing of lightweight and high-strength polymer-derived SiOC ceramics, *Virtual Phys. Prototyp.* 15 (2020) 163–177.
- [34] M. Shen, W. Qin, B. Xing, W. Zhao, S. Gao, Y. Sun, T. Jiao, Z. Zhao, Mechanical properties of 3D printed ceramic cellular materials with triply periodic minimal surface architectures, *J. Eur. Ceram. Soc.* 41 (2021) 1481–1489.
- [35] W. Zhao, C. Wang, B. Xing, M. Shen, Z. Zhao, Mechanical properties of zirconia octet truss structures fabricated by DLP 3D printing, *Mater. Res. Express* 7 (2020), 085201.
- [36] H.A. Schwarz, *Gesammelte Mathematische Abhandlungen*, Vol. 1, Springer, Berlin, 1890.
- [37] L. Han, S. Che, An overview of materials with triply periodic minimal surfaces and related geometry: from biological structures to self-assembled systems, *Adv. Mater.* 30 (2018) 1705708.
- [38] O. Al-Ketan, R.K. Abu Al-Rub, Multifunctional mechanical metamaterials based on triply periodic minimal surface lattices, *Adv. Eng. Mater.* 21 (2019) 1900524.
- [39] S. Wang, Y. Jiang, J. Hu, X. Fan, Z. Luo, Y. Liu, L. Liu, Efficient representation and optimization of TPMS-based porous structures for 3D heat dissipation, *Comput. Aided Des.* 142 (2022), 103123.

- [40] R.S. Ambekar, B. Kushwaha, P. Sharma, F. Bosia, M. Fraldi, N.M. Pugno, C. S. Tiwary, Topologically engineered 3D printed architectures with superior mechanical strength, *Mater. Today* 48 (2021) 72–94.
- [41] O. Al-Ketan, M. Pelanconi, A. Ortona, R.K. Abu Al-Rub, Additive manufacturing of architected catalytic ceramic substrates based on triply periodic minimal surfaces, *J. Am. Ceram. Soc.* 102 (2019) 6176–6193.
- [42] Y. Yao, W. Qin, B. Xing, N. Sha, T. Jiao, Z. Zhao, High performance hydroxyapatite ceramics and a triply periodic minimum surface structure fabricated by digital light processing 3D printing, *J. Adv. Ceram.* 10 (2021) 39–48.
- [43] L. Zhang, S. Feih, S. Daynes, S. Chang, M.Y. Wang, J. Wei, W.F. Lu, Pseudo-ductile fracture of 3D printed alumina triply periodic minimal surface structures, *J. Eur. Ceram. Soc.* 40 (2020) 408–416.
- [44] J. Bauer, S. Hengsbach, I. Tesari, R. Schwaiger, O. Kraft, High-strength cellular ceramic composites with 3D microarchitecture, *Proc. Natl. Acad. Sci. U. S. A* 111 (2014) 2453–2458.
- [45] H. Mei, R. Zhao, Y. Xia, J. Du, X. Wang, L. Cheng, Ultrahigh strength printed ceramic lattices, *J. Alloy. Compd.* 797 (2019) 786–796.
- [46] P. Colombo, Mechanical properties of silicon oxycarbide ceramic foams, *J. Am. Ceram. Soc.* 84 (2001) 2245–2251.
- [47] H. Elsayed, A. Chmielarz, M. Potoczek, T. Fey, P. Colombo, Direct ink writing of three dimensional Ti₂AlC porous structures, *Addit. Manuf.* 28 (2019) 365–372.
- [48] J. Gonzalez-Julian, S. Onrubia, M. Bram, C. Broeckmann, R. Vassen, O. Guillou, High-temperature oxidation and compressive strength of Cr₂AlC MAX phase foams with controlled porosity, *J. Am. Ceram. Soc.* 101 (2018) 542–552.
- [49] M. Belmonte, M. Koller, J.J. Moyano, H. Seiner, P. Miranzo, M.I. Osendi, J. González-Julián, Multifunctional 3D-printed cellular MAX-phase architectures, *Adv. Mater. Technol.* 4 (2019) 1900375.